

# Identifying Absorbing Aerosols Above Clouds From the Spinning Enhanced Visible and Infrared Imager Coupled With NASA A-Train Multiple Sensors

Ian Chang and Sundar A. Christopher

**Abstract**—Geostationary satellite data from the Spinning Enhanced Visible and Infrared Imager (SEVIRI) in conjunction with A-Train data are used to develop an algorithm for detecting biomass-burning smoke aerosols above closed-cell stratocumulus (Sc) clouds. The detection relies on spectral signatures, textural characteristics, and time-dependent spectral variation of SEVIRI data. A-Train data including the Ozone Monitoring Instrument (OMI) and the Cloud-Aerosol Lidar with Orthogonal Polarization (CALIOP) are used as reference data for the SEVIRI algorithm development. The 15-min repeat cycle of SEVIRI provides the capability for identifying smoke above closed-cell Sc with an OMI aerosol index value exceeding 0.5 and a cloud optical thickness greater than 6 at 0.81  $\mu\text{m}$ . The user accuracy of this algorithm is  $\sim 49\%$  when using only spectral signature and textural tests. When incorporating the “temporal consistency” tests into the algorithm, the user accuracy increases to  $\sim 65\%$ . The producer accuracy is over  $\sim 77\%$ , implying that the SEVIRI algorithm generally identifies smoke above clouds when CALIOP also identifies the same feature at the collocated pixel. However, CALIOP has the tendency to underestimate the presence of thin smoke aerosols above liquid clouds during daytime. This algorithm can be used to detect and study the daytime variation of smoke above liquid clouds.

**Index Terms**—Aerosols above clouds, algorithm, NASA A-Train, Spinning Enhanced Visible and Infrared Imager (SEVIRI).

## I. INTRODUCTION

THE representation of aerosols, clouds, and aerosol-cloud radiative effects remains highly uncertain, restricting the reconstruction of past climate and the prediction of future climate change [1]. The radiative forcing by anthropogenic aerosols due to scattering and absorption of shortwave (SW) radiation is known as the aerosol direct radiative forcing [2]. The aerosol direct radiative effect is defined as the difference between radiative fluxes in the absence and presence of aerosols [3]. The term “forcing” emphasizes perturbations stemming from anthropogenic sources [4]. The aerosol direct radiative forcing in cloud-free regions generally leads to a cooling (i.e.,

Manuscript received November 24, 2014; revised June 3, 2015 and August 27, 2015; accepted November 20, 2015. Date of publication March 30, 2016; date of current version April 27, 2016. This work was supported by NASA’s CALIPSO and Radiation Sciences programs.

I. Chang is with the Department of Atmospheric Science, University of Alabama in Huntsville, Huntsville, AL 35805 USA (e-mail: ian.chang@nsstc.uah.edu).

S. A. Christopher is with the Department of Atmospheric Science, University of Alabama in Huntsville, Huntsville, AL 35805 USA, and also with the Earth System Science Center, University of Alabama in Huntsville, Huntsville, AL 35805 USA.

Color versions of one or more of the figures in this paper are available online at <http://ieeexplore.ieee.org>.

Digital Object Identifier 10.1109/TGRS.2015.2513015

negative forcing) at top-of-atmosphere (TOA) [5], [6]. This forcing reduces surface temperatures since aerosols reflect more solar radiation than the surface (except for bright surfaces such as desert and snow). However, the aerosol direct radiative forcing in cloudy regions becomes more complex because aerosols could occur either above, below, or in the vicinity of clouds, complicating the estimation of radiative forcing. Moreover, cloud coverage below absorbing aerosols also influences both signs and magnitudes of the direct radiative effect at TOA [7].

The method of aerosol absorption detection using satellite UV observations was developed by P. K. Bhartia at the NASA Goddard Space Flight Center [8] and first documented by Hsu *et al.* [9] using reflectivity differences between two near-UV channels from the Nimbus-7 Total Ozone Mapping Spectrometer. Quantification of aerosol absorption has been conducted by Torres *et al.* [10] in a theoretical framework using the “residual method” based on the departure of the observed spectral differences in near-UV radiances from that of a molecular atmosphere. Hsu *et al.* [11] estimated radiative effects of smoke aerosols above clouds over southeast Asia using UV aerosol index (AI) as an indicator of smoke presence above cloud decks.

Inversion approaches from polarization measurements provide the capability for retrieving above-cloud aerosol optical thicknesses (AOTs). Waquet *et al.* [12], [13] pioneered a novel strategy for retrieving above-cloud fine-mode AOTs using polarized phase function at forward scattering angles from the POLarization and Directionality of the Earth’s Reflectances (POLDER). Simultaneous retrieval of AOT and cloud optical thickness (COT) has been conducted using inversion methods from near-UV radiances in the Ozone Monitoring Instrument (OMI) [14] and from visible (VIS)/near-infrared (NIR) color ratio techniques in the Moderate Resolution Imaging Spectroradiometer (MODIS) [15]. Such an approach has also been applied to simultaneously retrieve the aerosol absorption optical thickness and the underlying COT from POLDER measurements [16]. Using the DISORT radiative transfer model (RTM), Meyer *et al.* [17] performed corrections on low COT bias from overlying absorbing aerosols for August and September between 2006 and 2011 over the southeast Atlantic. They noted that adjusting for above-cloud aerosol attenuation at 0.86  $\mu\text{m}$  increases the regional mean COT by  $\sim 6\%$  relative to the existing standard MODIS cloud product (i.e., MOD06 and MYD06). Most recently, Meyer *et al.* [18] developed a technique to simultaneously retrieve above-cloud AOT and underlying liquid cloud optical and microphysical properties [i.e., COT and cloud effective radius ( $r_e$ )] by utilizing six MODIS channels ranging from VIS to SW infrared (SWIR)

wavelengths. Their look-up table (LUT) covered AOT, COT, and  $r_e$  using an optimal estimation method. The Cloud-Aerosol Lidar with Orthogonal Polarization (CALIOP), an active spaceborne lidar, also provides the capability for retrieving above-cloud AOT using 532- and 1064-nm channels. Various AOT retrieval approaches have been introduced on CALIOP such as the extinction to backscatter ratio technique [19], [20], the color ratio technique [21], and the depolarization ratio approach [22]. Intersensor comparison among these sensors has revealed consistent above-cloud AOT retrievals. However, the CALIOP 532 nm has shown to underestimate the above-cloud AOT due to the solar background illumination, causing a lower signal-to-noise ratio during daytime retrieval [16], [23]–[25].

Multisensor applications have also been performed in several studies. Alfaro-Contreras *et al.* [26] assessed the low COT bias due to smoke aerosols above clouds by collocating the OMI AI, CALIOP, and MODIS. They further compared the standard MODIS COT, derived from the 0.86- $\mu\text{m}$  channel, with the MODIS supplementary product (derived mainly from the SWIR 1.64- $\mu\text{m}$  channel). Both products were then referenced to COT at 0.646  $\mu\text{m}$ . Since the VIS channel is more sensitive to smoke attenuation than the NIR channel, the retrieved COT differences between these two channels yield the bias associated with smoke above clouds. They indicated that, for OMI AI exceeding 1, the low COT bias ranges between 10% and 20% at 0.86  $\mu\text{m}$  for smoke above clouds over the south Atlantic. A negative semidirect radiative forcing results in a thickening of stratocumulus (Sc) clouds due to overlying smoke aerosols based on A-Train measurements [27]. Wilcox [28] found a net positive radiative forcing of 0.3  $\text{Wm}^{-2}$  for smoke above clouds between the direct and semidirect radiative forcing. The direct radiative effects of absorbing aerosols above clouds are also sensitive to the optical thickness of absorbing aerosols. Zhang *et al.* [29] implemented a technique to estimate absorbing (smoke and polluted dust) aerosol-above-cloud direct radiative effect using CALIOP and MODIS. They found a direct radiative effect of  $\sim 30.9 \text{ Wm}^{-2}$  after making an adjustment to the CALIOP AOT's low bias by a factor of 5 [24].

The aforementioned studies have improved our understanding of above-cloud aerosol radiative effects. However, the temporal resolution of A-Train satellites is limited to one daytime overpass over a particular location per day, thereby inhibiting aerosol-above-cloud studies on a subdaily scale. While CALIOP has enabled a vertical viewing capability of aerosols above clouds, one of its major shortcomings pertains to its near-nadir viewing restrictions with a 16-day repeat cycle [19]. Such limitations hamper extensive horizontal spatial analyses of aerosols above clouds. Given the high temporal evolution in the properties of aerosols [30], monitoring the diurnal variation of the presence of aerosols above clouds will advance our understanding of short-term aerosol-above-cloud characteristics. Over the southeast Atlantic, the Spinning Enhanced Visible and Infrared Imager (SEVIRI) aboard the Meteosat Second Generation (MSG) satellite, located at the prime meridian above the equator, serves as the geostationary satellite platform for this region [31].

Numerous studies have utilized SEVIRI for feature detection that relies heavily on the high-temporal-resolution satellite data. For example, Derrien *et al.* [32] implemented a temporal differencing technique to identify clouds at high solar zenith angles (during sunset and sunrise). SEVIRI's high temporal resolution

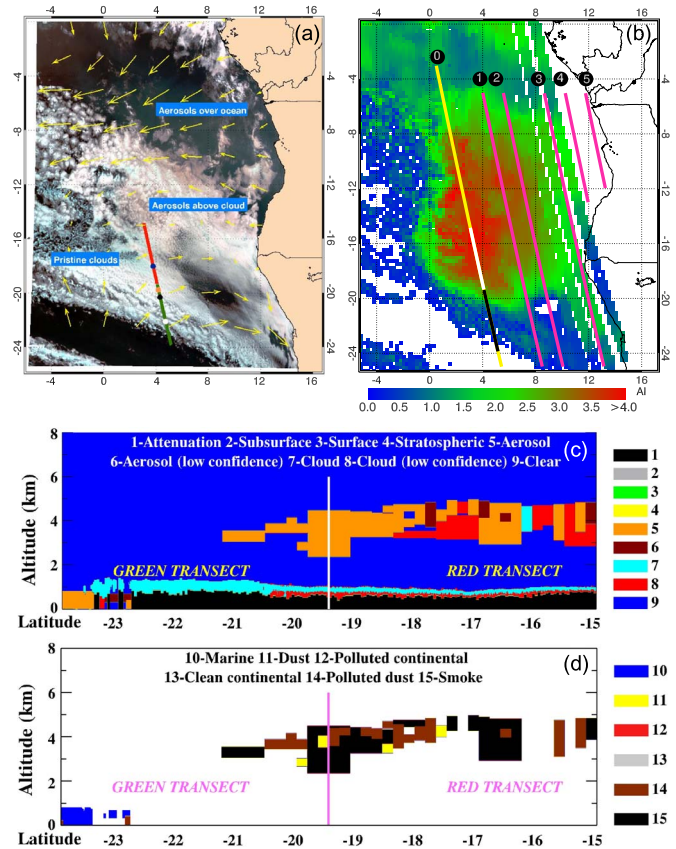


Fig. 1. (a) RGB composite from SEVIRI with a CALIOP overpass in green and red on August 13, 2006. Yellow arrows represent wind vectors at 850 hPa. Filled circles along the CALIOP overpass correspond to pixel locations in Fig. 6. (b) OMI UV AI at 1315Z on this day. The black (white) line represents the CALIOP overpass along the green (red) line in (a). The pink lines represent CALIOP overpasses that were used for uncertainty analysis for the selected case days. (c) VFM feature layers from CALIOP. (d) Aerosol subtype layers from CALIOP. In both (c) and (d), green and red transects correspond to the CALIOP overpass in (a).

has also provided capabilities for monitoring dust storm outbreaks in the Mediterranean region and the Arabian Peninsula [33], detecting and tracking volcanic ash [34], [35], and developing a fire detection algorithm over Africa [36]. The present study develops a method to identify smoke above closed-cell Sc using SEVIRI's multispectral, textural, and temporal characteristics. The condition that mostly resembles plane-parallel approximation in radiative transfer calculations is the extensive coverage of closed-cell Sc, so accurately identifying this feature is critical. The algorithm can be used to study the diurnal variation of smoke above Sc at a high temporal resolution. To keep the scope manageable, this study only concentrates on the algorithm development of smoke above closed-cell Sc detection. A future study will assess their daytime variations.

## II. STUDY AREA

An example of absorbing aerosols above clouds over the southeast Atlantic from different sensors is shown in Fig. 1. Fig. 1(a) shows a red-green-blue (RGB) three-band overlay of a SEVIRI image on August 13, 2006 at 1330Z over the southeast Atlantic Ocean. The central wavelengths of the red channel, the green channel, and the blue channel are 1.64, 0.81, and 0.64  $\mu\text{m}$ , respectively. Yellow arrows depict wind vectors at 850 hPa, which is the nearest pressure level from the cloud top

pressure. The maximum wind speed ( $10.2 \text{ ms}^{-1}$ ) corresponds to the longest vector on this image, which is located at the bottom right of this image. Pristine clouds appear as white since they are spectrally flat given their nonselective absorbing nature [37]. The light bluish regions are either cloud edges or thin clouds due to lower NIR reflectance at cloud edges [38]. The tannish discoloration of clouds occurs as a result of smoke attenuation in the green channel and the blue channel [15], [17], [26].

The southeast Atlantic is dominated by high biomass-burning aerosol loadings and semipermanent Sc during austral winter (June to September) [27], [28], [39]. The algorithm in this study is specifically designed for detecting smoke above closed-cell Sc, where clouds are characterized with ascending motion at the cell center and descending motion at the edge of the cell. This cloud type mostly appears over the eastern portion of ocean basins where a relatively cooler ocean current prevails. On the contrary, open-cell Sc is dominated by descending motion at the cell center and ascending motion at their edges [40], [41]. The large contrast in both reflectance and temperature properties in open-cellular convective regions results in high uncertainty for their detection as opposed to a more homogenous reflectance and temperature associated with closed-cell Sc. While this study focuses on aerosols originating from biomass burning in southern Africa, aerosols from South America could be transported eastward [42], [43] to cause potential intercontinental aerosol mixing. However, the frequency of such a mixing above liquid clouds in the southeast Atlantic remains uncertain [18] and is left for future investigations. The remainder of this study will focus on detecting smoke aerosols (originated from southern Africa) above clouds associated with closed-cellular convection.

### III. DATA AND METHODS

The A-Train data sets are coupled with SEVIRI (3-km nadir resolution) [31] to leverage an algorithm for detecting smoke above closed-cell Sc. This imager consists of 11 spectral channels (three solar channels and eight thermal channels) and a broadband high-resolution visible channel. The algorithm undergoes three major processes at a pixel level. We begin by using spectral thresholds to screen for smoke above low-level liquid clouds. Next, we perform a textural analysis to screen for cloud center and cloud edges. Finally, we apply temporal tests to screen for close-cell Sc. The eventual algorithm aims to identify smoke above closed-cell Sc at a pixel level. A-Train data including OMI AI and CALIOP lidar information will serve as a benchmark for the algorithm development. Detecting smoke above thin clouds or above cloud edges is beyond the scope of this study.

The UV AI data are obtained from Version 3 of OMI/Aura Level 2 near-UV Aerosol data product (OMAERUV\_V003). This index is calculated from the residual quantity based on the logarithm of the ratio of the measured radiances to the model-calculated radiances for a molecular-exclusive atmosphere. It has a spatial resolution of  $13 \text{ km} \times 24 \text{ km}$  at nadir [14]. Given the high uncertainty of identifying aerosols with low AI values [10], only AI values above 0.5 are identified as absorbing aerosols in this study. This threshold has also been adopted in Yu *et al.* [39] for above-cloud AOT assessment and in Feng and Christopher [44] for studying radiative effects of absorbing aero-

sols above clouds. Fig. 1(b) illustrates OMI AI for August 13, 2006, over the southeast Atlantic. Strong UV absorption can be seen at the center of this image as indicated by AI values exceeding 4. Torres *et al.* [14] noted a high sensitivity between the AI and the aerosol-cloud separation distance, particularly for absorbing aerosols above thin clouds with high separation distance. Another uncertainty in the interpretation of AI arises from the wavelength-dependent absorption AOT attributed to the aerosol single scattering albedo and the Angström absorption exponent. Note that this study merely focuses on detecting the presence of smoke aerosols above clouds. Assessing the strength of aerosol absorption above clouds is beyond the scope of the present study.

We also assess vertical distributions of clouds and aerosols via CALIOP onboard the Cloud-Aerosol Lidar and Infrared Pathfinder Satellite Observations (CALIPSO). Specifically, we use Level 2 Version 3.01 cloud layer and aerosol layer detection products at 5-km horizontal resolution [19], [45]. Additionally, the CALIOP Level 2 Vertical Feature Mask (VFM) and the aerosol subtype [46] have been used to screen for columns that exclusively contain smoke above clouds within each of the 5-km cloud and aerosol layer horizontal domain. The VFM and the aerosol subtype have a horizontal resolution of  $\sim 333 \text{ m}$  and a vertical resolution of 30 m between altitudes of  $-0.5$  and 8.2 km. Only a high confidence of aerosol and cloud detection is considered in this study. To eliminate possible mixings between aerosols and clouds within a vertical column, we enforce a 300-m minimum vertical separation distance between the smoke base and the cloud top. Since the standard VFM is generated from the 532-nm channel, the geometrical thickness of the smoke layer tends to be underestimated during daytime due to solar background illumination [17], [25], [47]. The underestimation of the geometrical thickness of smoke suggests that the smoke base may be much closer to the cloud top than the smoke base indicated by the VFM data. Using the VFM derived from the 1064-nm channel may be an alternative solution to detecting thin aerosols. However, the VFM at 1064 nm is unavailable to users, and its derivation is beyond the scope of this study. Ultimately, our goal is to confirm the presence of smoke above clouds from SEVIRI when CALIOP identifies the same feature. Fig. 1(c) shows the CALIOP feature layer, and Fig. 1(d) shows the aerosol subtype along the green line and the red line in Fig. 1(a). Since this study focuses on identifying smoke above clouds, we only select the aerosols that consist of only smoke aerosols within the entire 5-km aerosol feature layer.

The Aqua-MODIS Level 2 Collection 6 cloud product (MYD06) at 1-km nadir resolution is used to obtain COT and  $r_e$  [48] along the CALIOP overpass. While the OMI footprint exceeds any given MODIS footprint, we collocated the OMI pixel closest to the MODIS cloud pixel to obtain the aerosol absorption strength. Thus, an OMI footprint potentially serves as a collocation pixel for multiple SEVIRI, CALIOP, and MODIS pixels. Note that the present study aims to develop an algorithm for detecting smoke above closed-cell Sc on SEVIRI rather than deriving an algorithm for detecting aerosols of various AOTs above clouds of various COTs. However, an LUT for simultaneous AOT and COT retrievals for smoke above clouds is created for developing spectral thresholds (see Section IV). Low COT biases due to overlying smoke attenuation in the MYD06 product means that the minimum COT

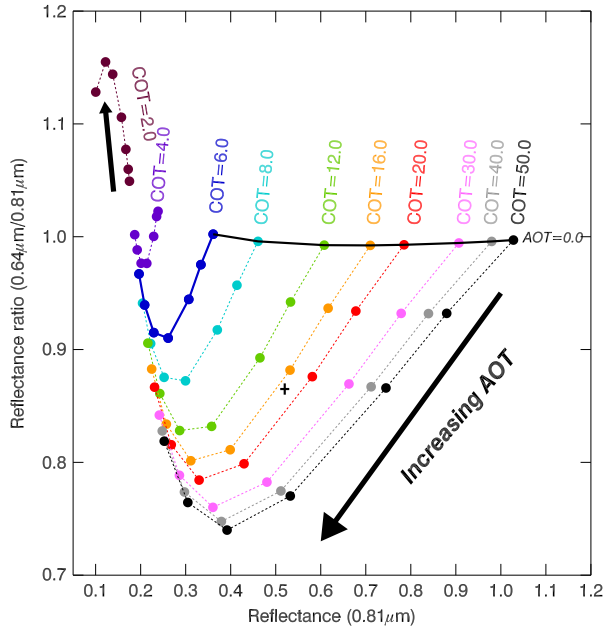


Fig. 2. LUT showing the simultaneous AOT and COT retrievals of smoke above clouds based on SEVIRI reflectance channels. The input parameters of the aerosol and cloud properties are outlined in Table I. Arrows indicate the direction to which the AOT increases in an interval of 0.0, 0.5, 1.0, 2.0, 3.0, 4.0, and 5.0. The black solid line connects various COTs in the absence of aerosols (i.e., AOT = 0.0). Dashed lines connect AOTs of the same COTs. The two solid lines indicate spectral thresholds for the identification of absorbing aerosols above clouds with COT  $\geq 6$ .

of this algorithm is likely the absolute minimum COT value that is valid for user applications. The presence of smoke above clouds does not cause a noticeable  $r_e$  retrieval bias since its retrieval depends on the SWIR (i.e., 1.64  $\mu\text{m}$ ), which is mostly transparent to submicrometer smoke aerosols [17], [18], [26].

#### IV. RADIATIVE TRANSFER CALCULATIONS

To guide the selection of spectral thresholds in the SEVIRI algorithm, simultaneous retrievals of AOT and COT are performed using the Santa Barbara DISORT Atmospheric Radiative Transfer program [49]. This retrieval technique relies on the reflectance ratio of the 0.64- $\mu\text{m}$  ( $R_{0.64}$ ) reflectance to the 0.81- $\mu\text{m}$  ( $R_{0.81}$ ) reflectance as a function of  $R_{0.81}$  (Fig. 2), which was developed by Jethva *et al.* [15] for MODIS. Likewise, this approach has also been applied to simultaneously retrieve absorption AOT and COT using radiances from OMI [14] and POLDER [16]. We used reflectance values at 0.64  $\mu\text{m}$  instead of those at 0.47  $\mu\text{m}$  as in Jethva *et al.* [15] since 0.64  $\mu\text{m}$  is the shortest available wavelength on SEVIRI. The details of the input parameters are outlined in Table I. Input aerosol properties follow the AERONET Level 2.0 observations at Mongu, Zambia, on August 13, 2006.

Spectral thresholds for smoke above clouds are identified on the spectral decision surface in Fig. 2. The results from the RT calculations show that smoke above clouds of COT = 2 mainly induce scattering effect with AOT retrieval highly sensitive to the changes in reflectance ratios. In contrast, smoke aerosol above clouds of COT  $\geq 6$  clearly cause absorbing effects with weak sensitivity to the changes in reflectance ratios during AOT retrieval. Both  $R_{0.81}$  and  $R_{0.64}/R_{0.81}$  decrease with an increasing AOT, indicating that attenuation of reflectance by

smoke occurs at both wavelengths. The attenuation, however, is greater at the 0.64  $\mu\text{m}$  than at 0.81  $\mu\text{m}$ . These trends are consistent with the LUT in Jethva *et al.* [15].

Given the complexity of AOT and COT retrievals below COT < 6, smoke-above-cloud detection in this study focuses on smoke above clouds of COT  $\geq 6$ . Spectral thresholds are based on the region in the spectral decision surface that is simultaneously less than the second-order polynomial along COT = 6 (blue curve) for various above-cloud AOTs and the second-order polynomial along AOT = 0 for COT  $\geq 6$  (black curve). Note that spectral thresholds vary depending on the model input parameters. Thus, Fig. 2 only represents an LUT smoke above-cloud detection for a specific set of aerosol properties, solar geometry, and viewing geometry. The second-order polynomial equations that are used for the LUT are shown in Fig. 7.

#### V. SEVIRI ALGORITHM

The goal of this study is to develop an algorithm for detecting smoke aerosols above closed-cell Sc on SEVIRI at pixel level using spectral, textural, and temporal characteristics. The algorithm development is organized as follows. Initially, we examine the spectral signatures of absorbing aerosols above clouds from SEVIRI's reflectance and thermal channels. A spectral decision surface is inferred from the LUT (see Section IV) to establish spectral thresholds. Next, we apply a textural test to assess the heterogeneity of a pixel and its neighboring pixels in order to remove cloud edges. When a pixel satisfies both spectral and textural tests, it undergoes a set of temporal tests for identifying smoke aerosols above closed-cell Sc.

Explanations on color differences are outlined with spectral signatures in Fig. 3, which illustrates the means and one standard deviation of reflectance for pristine clouds, aerosols above clouds with  $1 < \text{AI} < 2$ , and aerosols above clouds with  $\text{AI} > 2$  from all case days (Table II). The spectral signatures are based on pixels with  $R_{0.64} > 0.2$  to ensure that only thick clouds are chosen for the statistics. Note that pixels of all channels in Fig. 1(a) have also undergone histogram equalization in order to utilize all gray level values while attaining a quasi-uniform histogram over all reflectance values. This image enhancement technique provides a stronger distinction among features for better visualization since it gives the best representation of details at all ranges of reflectance values [50]. As an example, clouds have relatively higher reflectance values than most features in these three solar channels, so they tend to appear the brightest on an RGB composite [Fig. 3(a)]. When aerosols lie above clouds with  $1 < \text{AI} < 2$  [Fig. 3(b)], solar attenuation reduces the reflectance of both the green (VIS) and blue (NIR) channels by over 10% but by less than 5% in the red channel. The RGB composite after the entire image undergoes histogram equalization causes absorbing aerosols above clouds to appear as light gray. For  $\text{AI} > 2$  [Fig. 3(c)], aerosols reduce the reflectance of both green and blue, causing the image to appear as light brown.

The smoke outbreak on August 13, 2006 that emanated from central Africa and transported smoke toward the southeast Atlantic above marine Sc is chosen for the algorithm development due to the high range of AI values during A-Train overpass on that day. Fig. 1(b) shows that OMI AI reaches as high as 4 in the

TABLE I  
INPUT PARAMETERS IN THE RTM FOR SMOKE ABOVE CLOUDS. AEROSOL PROPERTIES ARE OBTAINED FROM AERONET OBSERVATIONS IN MONGU, ZAMBIA, ON AUGUST 13, 2006

RTM INPUT PARAMETERS				
SZA			30°	
VZA			20°	
RAA			55°	
Cloud height			1.5km	
Aerosol height			4km	
Cloud effective radius			10μm	
Surface reflectance			Sea water (default)	
Aerosol properties				
Wavelength (μm)	Single scattering albedo	Asymmetry parameter	Aerosol optical thickness	
0.44	0.84	0.64	0.45	
0.67	0.79	0.52	0.20	
0.86	0.76	0.46	0.12	
1.02	0.75	0.45	0.08	

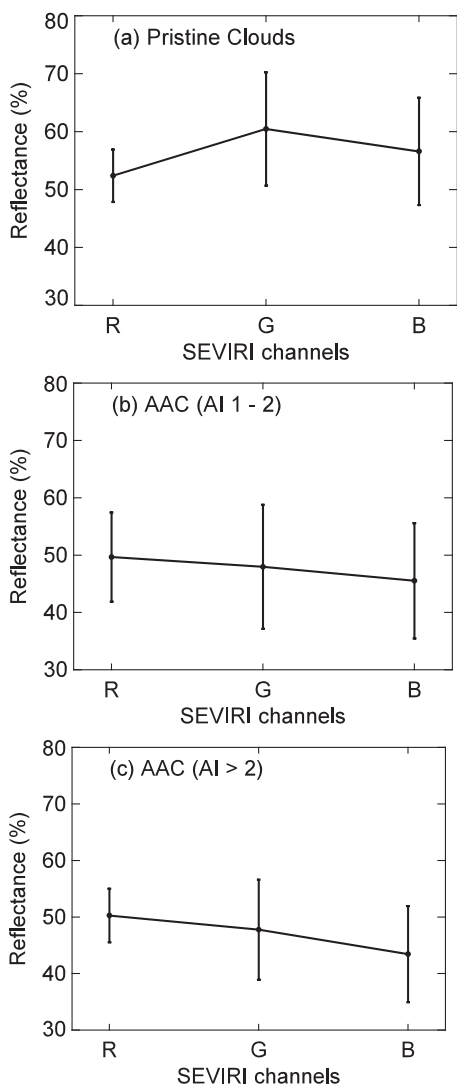


Fig. 3. Spectral signatures of (a) pristine clouds, (b) aerosols above clouds for  $1 < AI < 2$ , and (c) aerosols above clouds for  $AI > 2$  from all case days in terms of mean and one standard deviation in each channel. The red channel (R), the green channel (G), and the blue channel (B) have central wavelengths at 1.64, 0.81, and 0.64 μm, respectively.

middle of this image. However, we also perform an uncertainty analysis that includes cases where OMI AI values were less than 2.5 in this region. In this paper, CALIOP and OMI serve as a reference for validating aerosol and cloud presence.

A. Spectral Signatures

The initial stage of the algorithm is based on traditional spectral signatures from both reflectance and thermal channels. First, a pixel undergoes a temperature test at 10.8 μm ( $T_{10.8}$ ), which separates clouds from land and ocean.  $T_{10.8}$  for cloud tops tends to have a relatively lower temperature than that for ocean or land since this window wavelength detects either the Earth’s surface temperature under clear sky or the cloud-top temperature when clouds are present. A pixel is required to range between 280 and 295 K in order to isolate liquid clouds from either land, ocean, mixed-phase clouds, or ice clouds.

The next test involves a reflectance analysis, which is based on the spectral decision surface from the LUT in Fig. 2. As discussed earlier,  $R_{0.64}$  and  $R_{0.81}$  serve as the primary SEVIRI channels for separating pristine clouds from smoke above clouds since TOA reflectance at both wavelengths is sensitive to smoke scattering and absorption effects. Figs. 4 and 5 depict measurements along the green line and the red line in Fig. 1(a), respectively. These figures include information from CALIOP, OMI, MODIS, and SEVIRI. Cloud edges between latitudes of  $-23.2^\circ$  and  $-22.5^\circ$  are evidenced by  $r_e > 20 \mu\text{m}$  and  $COT < 2$  due to the emergence of multiple solutions for simultaneous low VIS and NIR reflection functions [38]. As shown in Fig. 1(a), this region is dominated by broken clouds, which supports the likelihood of cloud edges during the CALIOP overpass. Moreover, this region consists of mainly pristine clouds since OMI AI is below 0.5 and the VFM does not indicate any aerosols above low-level clouds in this region. The equatorward decrease of  $r_e$  and the increase of COT indicate the transition from the cloud edge toward the optically thick cloudy areas.

The southern tip of the green transect consists of ocean. Both  $R_{0.64}$  and  $R_{0.81}$  are less than 0.05 and  $R_{0.64} > R_{0.81}$  south of  $-23.5^\circ$  as shown in Fig. 4. At  $-23.5^\circ$ ,  $R_{0.64}$  and  $R_{0.81}$  are  $\sim 0.16$  and  $\sim 0.17$ , respectively. This reflectance combination suggests that the retrieval would take place outside the spectral thresholds. Fig. 5 shows a transect that consists of high aerosol

TABLE II  
NUMBER OF A-TRAIN PIXELS ALONG THE CALIOP TRACK THAT WERE USED FOR UNCERTAINTY ANALYSIS

CALIOP track no. (date)	Number of pixels
0 (13 August 2006)	490
1 (31 August 2006)	435
2 (24 August 2006)	446
3 (10 August 2006)	445
4 (18 July 2006)	178
5 (27 July 2006)	155
<b>Total</b>	<b>2149</b>

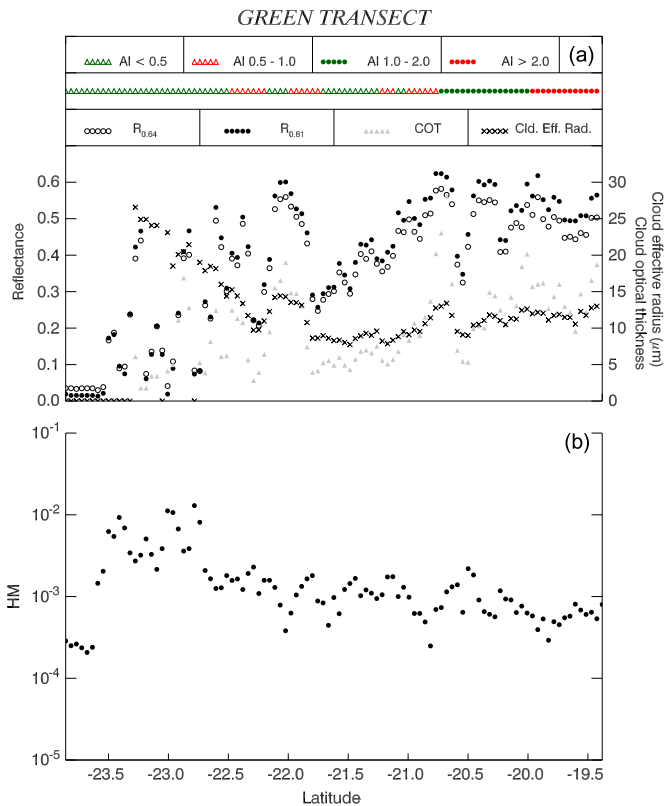


Fig. 4. (a) Green line in Fig. 1(a) illustrating  $R_{0.64}$  and  $R_{0.81}$  in SEVIRI (at 1330Z), COT and cloud effective radius (Cld. Eff. Rad.) from MYD06 (at 1335Z), and OMI AI (at 1315Z) grouped into four categories ( $< 0.5$ ,  $0.5-1.0$ ,  $1.0-2.0$ , and  $> 2.0$ ) on August 13, 2006. (b) HM based on a group of  $3 \times 3$  pixels from SEVIRI at the  $0.64\text{-}\mu\text{m}$  channel.

absorption above clouds as indicated by  $\text{AI} \geq 2$  throughout the entire transect. As an example, the reflectance ratio of  $\sim 0.865$  ( $R_{0.64}/R_{0.81} = 0.45/0.52$ ) and  $R_{0.81}$  of  $\sim 0.52$  at  $-18.0^\circ$  on this transect corresponds to the symbol “+” on the LUT in Fig. 2, yielding AOT and COT values of  $\sim 1.2$  and  $\sim 17$ , respectively.

### B. Textural Statistics

While spectral thresholds provide wavelength dependence of reflectance and temperature for smoke-above-cloud identification, the textural analysis reveals spatial characteristics of a group of pixels surrounding the pixel of interest. We perform several textural measures at  $0.64\ \mu\text{m}$  and find that the heterogeneity metric (HM) performs the best in isolating cloud centers from cloud edges according to our uncertainty analysis and visual inspection from all case days (Table II). The HM of a pixel is obtained by calculating the ratio of the standard deviation of  $R_{0.64}$  to the mean of  $R_{0.64}$  for a group of

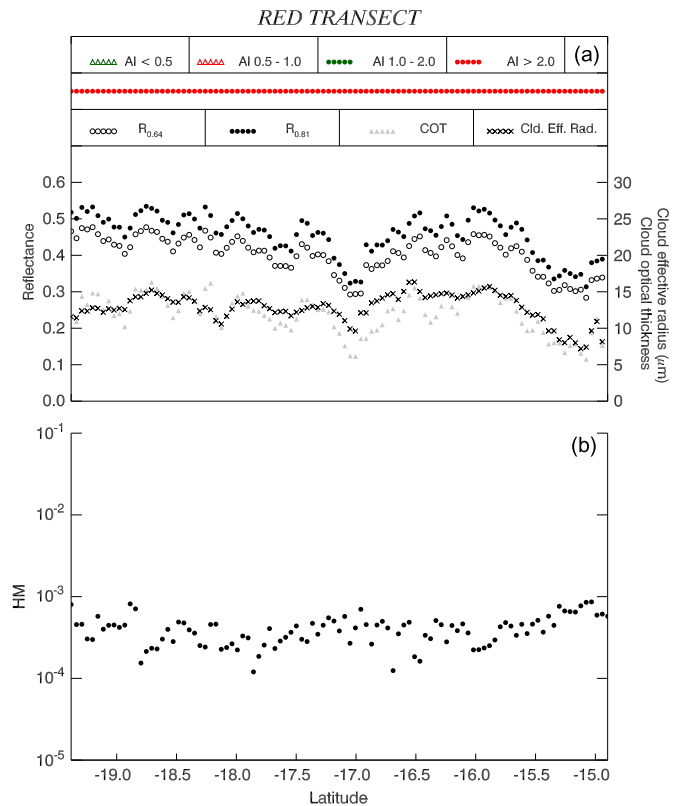


Fig. 5. As in Fig. 4, but for the red line in Fig. 1(a).

$3 \times 3$  pixels. The HM has also been applied to distinguish cloud edges from the center of extensive thick clouds in Liang *et al.* [51]. Such a task is not well captured by spectral thresholds alone.

Fig. 4(b) shows that the HM of the ocean is low ( $\sim 2.5 \times 10^{-4}$ ) because of its high homogeneity. Between  $-23.5^\circ$  and  $-22.7^\circ$ , the HM reaches as high as  $\sim 1.2 \times 10^{-2}$  due to a combination of cloud edges and open-cell Sc. From  $-22.7^\circ$  equatorward, the HM drops to  $\sim 10^{-3}$ , indicating that this region is more homogeneous than cloud edges. Fig. 5(b) reveals that the HM values are on the order of  $10^{-4}$ , indicating that reflected surfaces are fairly homogeneous throughout this domain. Based on our visual inspection and uncertainty analysis, a typical cloud center has an HM ranging from  $2 \times 10^{-4}$  to  $6 \times 10^{-3}$ . Values below this threshold are likely as homogeneous as ocean, while values above this threshold are likely cloud edges.

### C. Temporal Analysis

Using geostationary data allows one to assess the short-term evolution of clouds and aerosols because of their high

	T-30 (1300Z)			T-15 (1315Z)			T (1330Z)			T+15 (1345Z)			T+30 (1400Z)		
	AI = 0.0, COT = 15														
White circle	56	54	54	59	62	60	44	44	43	31	32	32	17	20	20
	50	<b>46</b>	45	59	<b>61</b>	62	51	<b>52</b>	51	36	<b>37</b>	37	23	<b>26</b>	26
	44	40	40	57	56	56	55	61	60	40	42	43	29	30	31
	AI = 1.0, COT = 14														
Black circle	47	42	38	55	55	54	46	52	56	25	39	49	27	25	22
	48	<b>41</b>	36	50	<b>48</b>	45	50	<b>55</b>	55	27	<b>42</b>	47	26	<b>28</b>	36
	50	42	39	45	41	37	51	55	51	36	48	54	28	35	47
	AI = 2.0, COT = 14														
Orange circle	47	48	51	50	49	53	46	48	50	50	51	51	51	53	54
	46	<b>47</b>	50	47	<b>48</b>	52	51	<b>50</b>	53	47	<b>48</b>	48	51	<b>54</b>	55
	48	50	52	47	50	53	50	52	55	46	49	51	50	51	51
	AI = 3.5, COT = 13														
Blue circle	43	43	43	46	45	45	43	43	43	42	42	42	41	43	44
	40	<b>39</b>	40	46	<b>46</b>	45	43	<b>43</b>	45	44	<b>44</b>	43	41	<b>43</b>	45
	37	36	37	43	44	45	46	45	46	44	45	44	43	44	44

Fig. 6. Temporal variations of  $R_{0.64}$  (in %) for the four colored circles along the CALIOP overpass in Fig. 1(a) during five consecutive SEVIRI snapshots with 15-min interval. The values in each small rectangle represent  $R_{0.64}$  of a SEVIRI pixel. The four black-shaded rectangles at 1330Z represent the SEVIRI pixels that are collocated with OMI AI, CALIOP, and MYD06 in both time and space. The boldface numbers at the center of each  $3 \times 3$  pixels outside 1330Z are collocated with A-Train overpass in location but not in time.

temporal (15-min) resolution. While both spectral signatures and textural analysis are essential for detecting smoke aerosols above cloud centers, scrutinizing a pixel over a period of time offers another dimension of analysis. In this case, the consistency of  $R_{0.64}$  over a time period provides the capability of synchronously assessing cloud coverage and cloud advection. Subsequently, one can determine pixels that have horizontally uniform cloud distributions (i.e., closed-cell Sc). For brevity, we refer to this set of tests as the “temporal consistency” tests.

The change in  $R_{0.64}$  at the four colored circles along the CALIOP overpass in Fig. 1(a) is presented in Fig. 6. The location of the four colored circles is selected based on similar MYD06 COTs with increasing AI. SEVIRI at 1330Z is collocated with A-Train at the nearest time and space. The white, black, orange, and blue circles are located at OMI AI values of 0, 1, 2, and 3.5, respectively. In the AI = 0 case (white circle), CALIOP only detects the presence of a cloud layer, with COT = 15 according to MYD06. At the collocated pixel, SEVIRI detects  $R_{0.64}$  of 52%. In the preceding times (i.e., T-30 and T-15) at the identical pixel location, the  $R_{0.64}$  values were 46% and 61% at 1300Z and 1315Z, respectively. It can be seen that  $R_{0.64}$  at this pixel location was rather unstable in terms of the change in magnitude. Moreover, the alternating change in the sign of  $R_{0.64}$  in each time interval clearly suggests that this region consists of a combination of broken clouds and cloud edges. In the succeeding times (i.e., T+15 and T+30),  $R_{0.64}$  dropped to 37% and 26%, respectively. While these visible reflectance values still warrant the presence of clouds, the cloud distribution over this region is nonuniform. Hence, this pixel unlikely represents a closed-cell Sc. Fig. 1(a) confirms that cumulus clouds dominate the white circled region.

The other three circles show examples of positive AI values above clouds. In the case of AI = 1.0 (black circle),  $R_{0.64}$  at the collocated pixel was 55% at 1330Z. In the preceding times,  $R_{0.64}$  increased from 41% at 1300Z to 48% at 1315Z. However, the reflectance plummeted to 42% at 1345Z and then dropped

down to 28% by 1400Z, indicating that this pixel was under broken cloud coverage. For AI = 2.0 (orange circle),  $R_{0.64}$  ranged between 47% and 54% at the collocated pixel during the five time frames. For AI = 3.5 (blue circle),  $R_{0.64}$  ranged between 39% and 46% at the collocated pixel during the five time frames. Both the orange and blue circles are located at an overcast closed-cell Sc region as shown in Fig. 1(a). Our findings suggest that closed-cell Sc is well represented when  $R_{0.64}$  changes by less than 25% in every 15-min interval during the four time intervals referencing from the time of higher  $R_{0.64}$  between each time interval. As an example, pixels over both the orange and blue circles satisfy the 25% criteria in all four time intervals. For the white circle, however,  $R_{0.64}$  change exceeded 25% between 1330Z and 1345Z and between 1345Z and 1400Z even though the two preceding time intervals changed by less than 25%. In this case, the white circle area would not be assigned as closed-cell Sc based on the temporal consistency thresholds.

Fig. 7 illustrates a series of tests that each SEVIRI pixel must undergo before being assigned as a smoke above closed-cell Sc pixel. A pixel will follow the solid arrow if it satisfies the criteria in a particular test; otherwise, it will follow the dashed line. For a pixel to be qualified as smoke above closed-cell Sc, it must pass the spectral, textural, and temporal consistency tests. Italic texts within each dashed box indicate features that a pixel may represent if a test is not satisfied. All thresholds have undergone iterative adjustments based on the uncertainty analysis and visual inspection over the five case days.

#### D. Algorithm Results

The results after applying the smoke above closed-cell Sc algorithm are shown in Fig. 8. The original RGB image prior to algorithm application is shown in Fig. 8(a) for readers’ reference, which is identical to Fig. 1(a) after removing all of the labels. The results from applying only the spectral thresholds

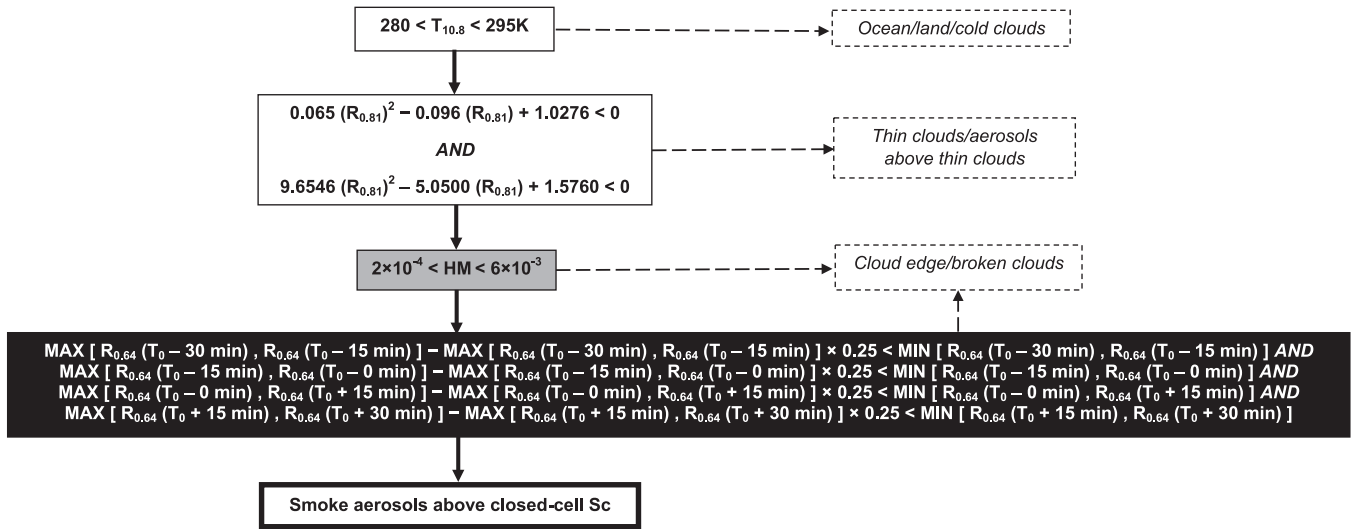


Fig. 7. Algorithm for detecting smoke above clouds using spectral signatures, textural analysis, and temporal consistency tests based on SEVIRI. Solid boxes are tests that each pixel must undergo starting from the top. The boxes in white, gray, and black are the spectral signature tests, the textural test, and the temporal consistency tests, respectively. When a pixel does not satisfy the criteria in a particular test, it will follow the dashed arrow, which shows the feature that it likely represents.

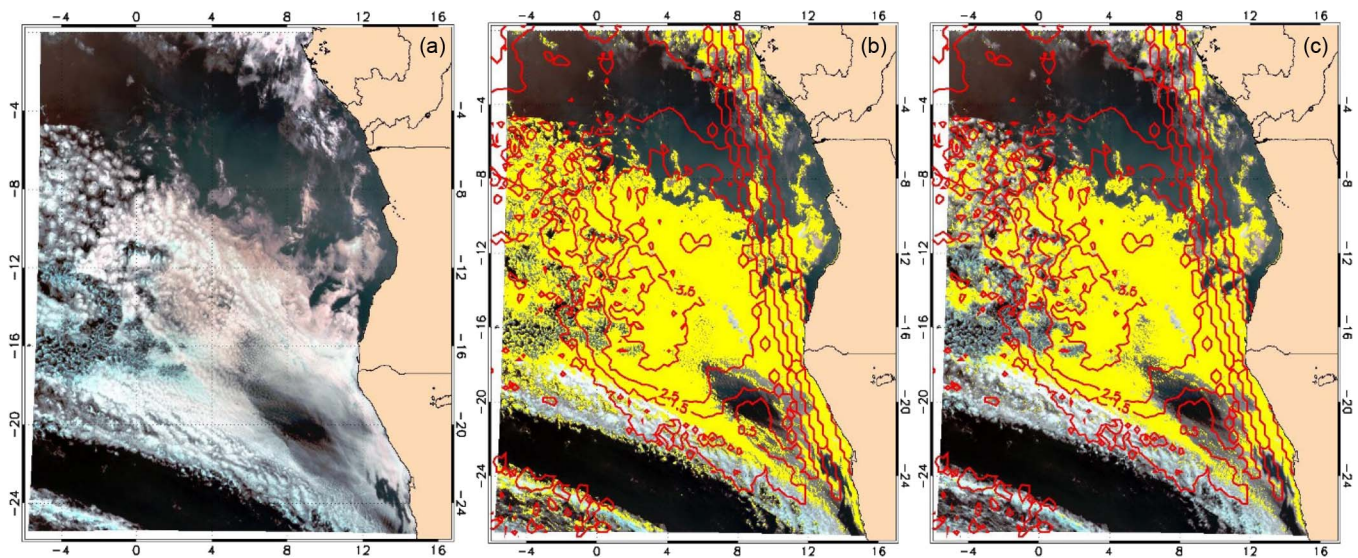


Fig. 8. (a) RGB image as in Fig. 1(a). (b) Results of SEVIRI-derived smoke above clouds based on spectral, textural, and temporal consistency tests. (c) Results of SEVIRI-derived smoke above closed-cell Sc based on spectral, textural, and temporal consistency tests. Red contours denote lines of equal OMI AI values starting from 0.5. The honeycomb-like contours along the coastlines result from row anomaly. Note that the OMI AI contours in both (b) and (c) are identical.

and textural statistics of the algorithm are presented in Fig. 8(b). The central portion of this image is classified as smoke above clouds, where OMI AI values exceed 0.5. However, smoke above clouds are assigned by the algorithm in the region bounded by 18–20° S and 0–4° W, where OMI AI values are below 0.5. In the southwestern corner of the image, a scattered amount of pixels is assigned as smoke above clouds, coinciding with a few AI = 0.5 contours. Fig. 8(c) shows results after incorporating the temporal consistency tests into the algorithm. The classification criteria become more stringent than spectral and textural tests alone since the temporal consistency tests determine if the pixel of interest is a closed-cell Sc. An examination of the synoptic weather map indicates that clouds in the southwestern portion of the image are likely associated with a cold front. Very few pixels satisfy the criteria for smoke above closed-cell Sc in this area after applying the

temporal consistency tests, affirming the soundness of applying the entire series of algorithm for smoke above closed-cell Sc detection.

## VI. UNCERTAINTY ANALYSIS

The uncertainty analysis is conducted using the CALIOP cloud and aerosol layer product, the VFM, and OMI AI as the reference data for comparison with the SEVIRI-derived smoke-above-cloud algorithm. The criteria for smoke above-cloud detection by CALIOP include the criteria discussed in Section III and OMI AI exceeding 0.5. For the pristine cloud detection case, the criteria of the reference data include CALIOP layers with clouds below 5 km, aerosol-free, OMI AI below 0.5, and SEVIRI  $R_{0.64}$  exceeding 0.2. The inclusion of SEVIRI in the reference data is required to ensure that both CALIOP cloud layers and a SEVIRI pixel agree on the cloud presence.

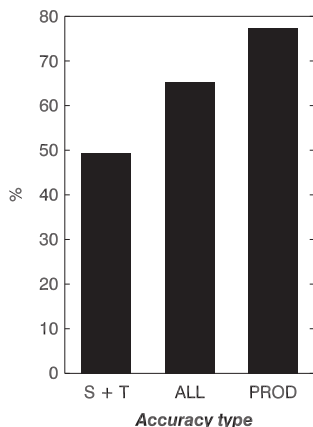


Fig. 9. Bar graph depicting the accuracies of SEVIRI-derived smoke above clouds. The “S + T” label denotes the user accuracy using only a combination of spectral and textural tests. The “ALL” label denotes the user accuracy for all (spectral, textural, and temporal consistency) tests. The “PROD” label denotes the producer accuracy for all tests.

The uncertainty analysis is presented in terms of a user accuracy and a producer accuracy. The user accuracy is defined as the percentage of SEVIRI pixels that are correctly identified as smoke above any cloud type rather than as pristine clouds when compared with the reference data. The producer accuracy is the percentage of reference data pixels that detect smoke above clouds and is also agreed by SEVIRI. Note that, since the cloud reference data (i.e., CALIOP) do not provide information on cloud types (i.e., open-cell or closed-cell), our uncertainty analysis is limited to smoke above clouds rather than smoke above closed-cell Sc. However, we will compare the accuracy between the inclusion and the exclusion of the temporal consistency tests to assess the impact of temporal information on the resulting accuracy.

The bar graph in Fig. 9 shows the user accuracy and the producer accuracy converted from a traditional error matrix (or confusion matrix). Using only the spectral signature and textural tests, the SEVIRI algorithm has identified 219 smoke above clouds pixels, with 108 pixels being verified by the reference data. Thus, the user accuracy for this scenario is  $\sim 49\%$  (see “S + T” in Fig. 9). When adding the temporal consistency tests in the SEVIRI algorithm, a total of 147 SEVIRI pixels have been identified as smoke above clouds. Among these 147 pixels, 96 pixels are being verified by the reference data, yielding a user accuracy of  $\sim 65\%$  (see “ALL” in Fig. 9). Hence, the increasing user accuracy after incorporating the temporal consistency tests suggests that the algorithm performs better at detecting smoke above closed-cell Sc than smoke above other cloud types.

As aforementioned, 96 pixels have been confirmed as smoke above clouds by both the reference data and the algorithm when the temporal consistency tests were included. In 28 collocated pixels, the reference data indicate smoke above clouds, while the SEVIRI algorithm detects either pristine clouds or smoke above thin clouds. As a result, the producer accuracy is  $\sim 77\%$  (see “PROD” in Fig. 9). Likewise, the producer accuracy when excluding the temporal consistency tests (spectral and textural only) is  $\sim 69\%$  (not shown). In summary, the SEVIRI algorithm generally identifies smoke above clouds when CALIOP also identifies the same feature at the collocated pixel. The producer accuracy exceeds the user accuracy regardless of the inclusion

of the temporal consistency tests since CALIOP has the tendency to underestimate the presence of thin smoke aerosols above liquid clouds during daytime [17], [25], [47]. We focus on the producer accuracy in this study since we aim to identify smoke above clouds provided that CALIOP also detects the same feature in the collocated region. Additionally, the temporal consistency tests also improve the accuracy because the closed-cell Sc is characterized with a more homogeneous background than cloud edges or cumulus clouds.

## VII. SUMMARY AND CONCLUSION

An algorithm for detecting smoke above closed-cell Sc has been developed for the SEVIRI data set, which relies on spectral signatures, textural statistics, and high-temporal-resolution capabilities. The southeast Atlantic is dominated by high biomass-burning smoke aerosol loadings and semipermanent Sc during austral winters, serving as a natural laboratory for developing the smoke above closed-cell Sc algorithm. The algorithm is generated by collocating the SEVIRI data with A-Train satellite sensors including MODIS, CALIOP, and OMI. CALIOP provides the vertical distributions of aerosols and clouds, while the OMI AI provides UV aerosol absorption above clouds.

The algorithm comprises the use of spectral signatures from both reflectance and thermal channels with prescribed thresholds. A spectral decision surface inferred from an LUT is generated to assign spectral thresholds for identifying smoke above clouds. This LUT relies on the reflectance ratio of  $R_{0.64}$  to  $R_{0.81}$  and provides the capability of synchronously retrieving AOT and COT. Importantly, this algorithm mainly detects smoke above clouds of  $COT \geq 6$  since identifying smoke above thin clouds is subject to high uncertainty. The HM, a textural analysis used in this study, distinguishes cloud edges from cloud center. Upon passing the spectral and textural tests, a pixel undergoes a set of temporal consistency tests, which inspects pixel consistency and homogeneity over a 60-min period in  $R_{0.64}$ .

The uncertainty analysis is based on the user accuracy and the producer accuracy from the five selected case days in 2006. The user accuracy is defined as the percentage of SEVIRI pixels that are correctly identified as smoke above clouds rather than as pristine clouds with respect to A-Train. The producer accuracy is defined as the percentage of reference pixels that are identified as smoke above clouds and is simultaneously agreed by SEVIRI. Results indicate that the user accuracy is  $\sim 49\%$  when only applying the spectral and textural tests and increases to  $\sim 65\%$  when incorporating the temporal consistency tests. The producer accuracy of the algorithm in this study is  $\sim 69\%$  ( $\sim 77\%$ ) when excluding (including) the temporal consistency tests, implying that the SEVIRI algorithm generally identifies smoke above clouds when CALIOP also identifies the same feature at the collocated pixel. However, when a SEVIRI pixel is classified as smoke above cloud, CALIOP only agrees with the collocated SEVIRI pixel  $\sim 49\%$  of the time. These findings are anticipated since CALIOP has the tendency to underestimate the presence of thin smoke aerosols above liquid clouds during daytime [17], [25], [47]. The accuracy in the present study focuses on the producer accuracy since our goal is to validate the presence of smoke above clouds from SEVIRI provided that CALIOP also identifies the same feature at the

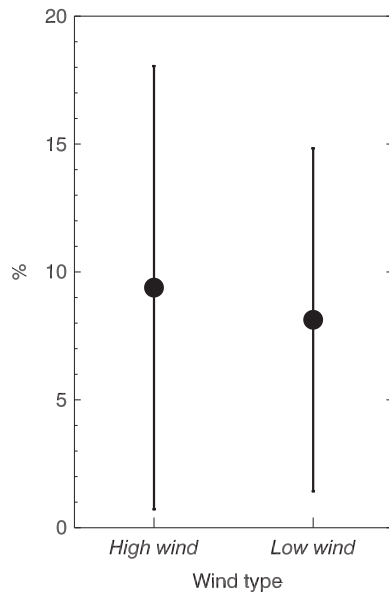


Fig. 10. Means and one standard deviation of the change in  $R_{0.64}$  between T-30 min and T+30 min for high- ( $> 6 \text{ ms}^{-1}$ ) and low- ( $< 5 \text{ ms}^{-1}$ ) wind events.

collocated pixel. Assessing the magnitude of CALIOP AOT underestimation is beyond the scope of this study.

This study presents a novel approach to identifying smoke above closed-cell Sc using spectral, textural, and temporal properties. The algorithm can be used to examine the spatiotemporal variation of smoke above closed-cell Sc at a subdaily scale from an observational standpoint. The upcoming field experiments such as CLOUD-Aerosol-Radiation Interactions and Forcing: Year 2016 (CLARIFY-2016), ObseRvations of Aerosols above CLouds and their intERactionS (ORACLES), and Layered Atlantic Smoke Interactions with Clouds (LASIC) will improve the understanding of radiative effects of absorbing aerosols above and within clouds in the southeast Atlantic. Data from these experiments will offer the validation of satellite retrievals and the documentation of uncertainties of RTM calculations in the field of radiative effects of absorbing aerosols above and within clouds.

#### APPENDIX

In a subset study, we used the NCEP Reanalysis 850 hPa wind data at  $2.5^\circ \times 2.5^\circ$  spatial resolution [52] to determine whether the magnitude of cloud advection has any influence on the magnitude of the change of reflectance. We hypothesize that reflectance would change less during the 60-min period under light-wind conditions relative to high-wind conditions since less clouds would pass over the same pixel area under light-wind conditions.

To examine the influence of wind speed on  $R_{0.64}$  change over cloudy conditions, pixels possessing  $R_{0.64}$  exceeding 20% for the 60-min period are assessed by computing the  $R_{0.64}$  difference between T-30 and T+30. The wind speed is categorized into two groups, namely, the high-wind ( $> 6 \text{ ms}^{-1}$ ) and the low-wind ( $< 5 \text{ ms}^{-1}$ ) types. A total of 683 (568) pixels are classified as high- (low-) wind category for the six days. Fig. 10 shows the statistics of  $R_{0.64}$  change over 60 min. In the high-wind category, the mean change of  $R_{0.64}$  between the two periods is  $9.4 \pm 8.7\%$ . In the low-wind

category this change drops to  $8.1 \pm 6.7\%$ . Since the means and the standard deviations of the two wind categories over the 60-min period are very similar, the changes in  $R_{0.64}$  associated with wind speeds appear to be an insignificant factor in our algorithm.

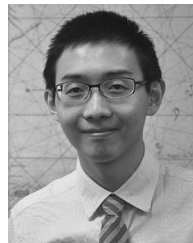
#### ACKNOWLEDGMENT

The authors would like to thank R. J. Swap for the discussions regarding intercontinental aerosol transport and the AERONET science program and the principal investigators for their effort in establishing and maintaining the Mongu, Zambia, site. The CALIOP data were obtained from the NASA Langley Research Center Atmospheric Science Data Center (<https://eosweb.larc.nasa.gov/JORDER/ceres.html>). The MODIS data were obtained from NASA Level 1 and Atmosphere Archive and Distribution System (<http://ladsweb.nascom.nasa.gov/data/>). The OMI data were obtained from NASA Goddard Earth Sciences Data and Information Services Center ([http://disc.sci.gsfc.nasa.gov/Aura/data-holdings/OMI/omaeruv\\_v003.shtml](http://disc.sci.gsfc.nasa.gov/Aura/data-holdings/OMI/omaeruv_v003.shtml)). The SEVIRI data were obtained from the European Organisation for the Exploitation of Meteorological Satellites Web interface (<https://eoportal.eumetsat.int/userMgmt/protected/dataCentre.faces>). The NCEP Reanalysis data were provided by the NOAA/OAR/ESRL PSD, Boulder, Colorado, USA, from their website at <http://www.esrl.noaa.gov/psd/>.

#### REFERENCES

- [1] R. A. Kahn, "Reducing the uncertainties in direct aerosol radiative forcing," *Surv. Geophys.*, vol. 33, no. 3/4, pp. 701–721, Jul. 2012.
- [2] S. K. Satheesh *et al.*, "A model for the natural and anthropogenic aerosols over the tropical Indian Ocean derived from Indian Ocean experiment data," *J. Geophys. Res. Atmos.*, vol. 104, no. D22, pp. 27 421–27 440, Nov. 1999.
- [3] N. G. Loeb and N. Manalo-Smith, "Top-of-atmosphere direct radiative effect of aerosols over global oceans from merged CERES and MODIS observations," *J. Clim.*, vol. 18, no. 17, pp. 3506–3526, Sep. 2005.
- [4] R. M. Hoff and S. A. Christopher, "Remote sensing of particulate pollution from space: Have we reached the promised land?" *J. Air Waste Manag. Assoc.*, vol. 59, no. 6, pp. 645–675, Jun. 2009.
- [5] A. Keil and J. M. Haywood, "Solar radiative forcing by biomass burning aerosol particles during SAFARI 2000: A case study based on measured aerosol and cloud properties," *J. Geophys. Res. Atmos.*, vol. 108, no. D13, p. 8467, Jul. 2003.
- [6] S. A. Christopher, D. V. Kliche, J. Chou, and R. M. Welch, "First estimates of the radiative forcing of aerosols generated from biomass burning using satellite data," *J. Geophys. Res. Atmos.*, vol. 101, no. D16, pp. 21 265–21 273, Sep. 1996.
- [7] D. Chand, R. Wood, T. L. Anderson, S. K. Satheesh, and R. J. Charlson, "Satellite-derived direct radiative effect of aerosols dependent on cloud cover," *Nat. Geosci.*, vol. 2, no. 3, pp. 181–184, Mar. 2009.
- [8] O. Torres and L. A. Remer, "History of passive remote sensing of aerosol from space," in *Aerosol Remote Sensing*, J. Lenoble, L. Remer, and D. Tanre, Eds. Berlin, Germany: Springer-Verlag, 2013, pp. 159–183.
- [9] N. C. Hsu *et al.*, "Detection of biomass burning smoke from TOMS measurements," *Geophys. Res. Lett.*, vol. 23, no. 7, pp. 745–748, Apr. 1996.
- [10] O. Torres, P. K. Bhartia, J. R. Herman, Z. Ahmad, and J. Gleason, "Derivation of aerosol properties from satellite measurements of backscattered ultraviolet radiation: Theoretical basis," *J. Geophys. Res. Atmos.*, vol. 103, no. D14, pp. 17 099–17 110, Jul. 1998.
- [11] N. C. Hsu, J. R. Herman, and S.-C. Tsay, "Radiative impacts from biomass burning in the presence of clouds during boreal spring in southeast Asia," *Geophys. Res. Lett.*, vol. 30, no. 5, p. 1224, Mar. 2003.
- [12] F. Waquet *et al.*, "Aerosol remote sensing over clouds using A-Train observations," *J. Atmos. Sci.*, vol. 66, no. 8, pp. 2468–2480, Aug. 2009.
- [13] F. Waquet *et al.*, "Retrieval of aerosol microphysical and optical properties above liquid clouds from POLDER/PARASOL polarization measurements," *Atmos. Meas. Tech.*, vol. 6, no. 4, pp. 991–1016, Apr. 2013.
- [14] O. Torres, H. Jethva, and P. K. Bhartia, "Retrieval of aerosol optical depth above clouds from OMI observations: Sensitivity analysis and case studies," *J. Atmos. Sci.*, vol. 69, no. 3, pp. 1037–1053, Sep. 2012.
- [15] H. Jethva, O. Torres, L. A. Remer, and P. K. Bhartia, "A color ratio method for simultaneous retrieval of aerosol and cloud optical thickness

- of above-cloud absorbing aerosols from passive sensors: Application to MODIS measurements," *IEEE Trans. Geosci. Remote Sens.*, vol. 51, no. 7, pp. 3862–3870, Jul. 2013.
- [16] F. Peers *et al.*, "Absorption of aerosols above clouds from POLDER/PARASOL measurements and estimation of their direct radiative effect," *Atmos. Chem. Phys.*, vol. 15, no. 8, pp. 4179–4196, Apr. 2015.
- [17] K. Meyer, S. Platnick, L. Oreopoulos, and D. Lee, "Estimating the direct radiative effect of absorbing aerosols overlying marine boundary layer clouds in the southeast Atlantic using MODIS and CALIOP," *J. Geophys. Res. Atmos.*, vol. 118, no. 10, pp. 4801–4815, May 2013.
- [18] K. Meyer, S. Platnick, and Z. Zhang, "Simultaneously inferring above-cloud absorbing aerosol optical thickness and underlying liquid phase cloud optical and microphysical properties using MODIS," *J. Geophys. Res. Atmos.*, vol. 120, no. 11, pp. 5524–5547, Jun. 2015.
- [19] D. M. Winker *et al.*, "Overview of the CALIPSO mission and CALIOP data processing algorithms," *J. Atmos. Ocean. Technol.*, vol. 26, no. 11, pp. 2310–2323, Nov. 2009.
- [20] S. A. Young and M. A. Vaughan, "The retrieval of profiles of particulate extinction from Cloud-Aerosol Lidar Infrared Pathfinder Satellite Observations (CALIPSO) Data: Algorithm description," *J. Atmos. Ocean. Technol.*, vol. 26, no. 6, pp. 1105–1119, Jun. 2009.
- [21] D. Chand *et al.*, "Quantifying above-cloud aerosol using spaceborne lidar for improved understanding of cloudy-sky direct climate forcing," *J. Geophys. Res. Atmos.*, vol. 113, no. D13, Jul. 2008, Art. ID D13206.
- [22] H. Yu *et al.*, "Quantification of trans-Atlantic dust transport from seven-year (2007–2013) record of CALIPSO lidar measurements," *Remote Sens. Environ.*, vol. 159, pp. 232–249, Mar. 2015.
- [23] D. M. Winker *et al.*, "The global 3-D distribution of tropospheric aerosols as characterized by CALIOP," *Atmos. Chem. Phys.*, vol. 13, no. 6, pp. 3345–3361, Mar. 2013.
- [24] H. Jethva, O. Torres, F. Waquet, D. Chand, and Y. Hu, "How do A-Train sensors intercompare in the retrieval of above-cloud aerosol optical depth? A case study-based assessment," *Geophys. Res. Lett.*, vol. 41, no. 1, pp. 186–192, Jan. 2014.
- [25] Z. Liu *et al.*, "Evaluation of CALIOP 532 nm aerosol optical depth over opaque water clouds," *Atmos. Chem. Phys.*, vol. 15, no. 3, pp. 1265–1288, Feb. 2015.
- [26] R. Alfaro-Contreras, J. Zhang, J. R. Campbell, R. E. Holz, and J. S. Reid, "Evaluating the impact of aerosol particles above cloud on cloud optical depth retrievals from MODIS," *J. Geophys. Res. Atmos.*, vol. 119, no. 9, pp. 5410–5423, May 2014.
- [27] E. M. Wilcox, "Stratocumulus cloud thickening beneath layers of absorbing smoke aerosol," *Atmos. Chem. Phys.*, vol. 10, no. 23, pp. 11 769–11 777, Dec. 2010.
- [28] E. M. Wilcox, "Direct and semi-direct radiative forcing of smoke aerosols over clouds," *Atmos. Chem. Phys.*, vol. 12, no. 1, pp. 139–149, Jan. 2012.
- [29] Z. Zhang *et al.*, "A novel method for estimating shortwave direct radiative effect of above-cloud aerosols using CALIOP and MODIS data," *Atmos. Meas. Tech.*, vol. 7, no. 6, pp. 1777–1789, Jun. 2014.
- [30] T. Takemura, T. Nakajima, O. Dubovik, B. N. Holben, and S. Kinne, "Single-scattering albedo and radiative forcing of various aerosol species with a global three-dimensional model," *J. Clim.*, vol. 15, no. 4, pp. 333–352, Feb. 2002.
- [31] J. Schmets *et al.*, "An introduction to Meteosat Second Generation (MSG)," *Bull. Amer. Meteorol. Soc.*, vol. 83, no. 7, pp. 977–992, Jul. 2002.
- [32] M. Derrien and H. L. Gléau, "Improvement of cloud detection near sunrise and sunset by temporal-differencing and region-growing techniques with real-time SEVIRI," *Int. J. Remote Sens.*, vol. 31, no. 7, pp. 1765–1780, Apr. 2010.
- [33] F. Sannazzaro *et al.*, "Identification of dust outbreaks on infrared MSG-SEVIRI data by using a robust satellite technique (RST)," *Acta Astronaut.*, vol. 93, pp. 64–70, Jan. 2014.
- [34] S. A. Christopher, N. Feng, A. Naeger, B. Johnson, and F. Marengo, "Satellite remote sensing analysis of the 2010 Eyjafjallajökull volcanic ash cloud over the North Sea during 4–18 May 2010," *J. Geophys. Res. Atmos.*, vol. 117, no. D20, Oct. 2012, Art. ID D00U20.
- [35] A. R. Naeger and S. A. Christopher, "The identification and tracking of volcanic ash using the Meteosat Second Generation (MSG) Spinning Enhanced Visible and Infrared Imager (SEVIRI)," *Atmos. Meas. Tech.*, vol. 7, no. 2, pp. 581–597, Feb. 2014.
- [36] G. J. Roberts and M. J. Wooster, "Fire detection and fire characterization over Africa using Meteosat SEVIRI," *IEEE Trans. Geosci. Remote Sens.*, vol. 46, no. 4, pp. 1200–1218, Apr. 2008.
- [37] M. Wang and W. Shi, "Cloud masking for ocean color data processing in the coastal regions," *IEEE Trans. Geosci. Remote Sens.*, vol. 44, no. 11, pp. 3196–3105, Nov. 2006.
- [38] T. Nakajima and M. D. King, "Determination of the optical thickness and effective particle radius of clouds from reflected solar radiation measurements. Part I: Theory," *J. Atmos. Sci.*, vol. 47, no. 15, pp. 1878–1893, Aug. 1990.
- [39] H. Yu *et al.*, "An integrated analysis of aerosol above clouds from A-Train multi-sensor measurements," *Remote Sens. Environ.*, vol. 121, pp. 125–131, Jun. 2012.
- [40] B. Stevens *et al.*, "Pockets of open cells and drizzle in marine stratocumulus," *Bull. Amer. Meteorol. Soc.*, vol. 86, no. 1, pp. 51–57, Jan. 2005.
- [41] E. M. Agee, T. S. Chen, and K. E. Dowell, "A review of mesoscale cellular convection," *Bull. Amer. Meteorol. Soc.*, vol. 54, no. 10, pp. 1004–1012, Oct. 1973.
- [42] A. S. Bachmeier and H. E. Fuelberg, "A meteorological overview of the TRACE A period," *J. Geophys. Res. Atmos.*, vol. 101, no. D19, pp. 23 881–23 888, Oct. 1996.
- [43] R. W. Talbot *et al.*, "Chemical characteristics of continental outflow over the tropical South Atlantic Ocean from Brazil and Africa," *J. Geophys. Res. Atmos.*, vol. 101, no. D19, pp. 24 187–24 202, Oct. 1996.
- [44] N. Feng and S. A. Christopher, "Measurement-based estimates of direct radiative effects of absorbing aerosols above clouds," *J. Geophys. Res. Atmos.*, vol. 120, no. 14, pp. 6908–6921, Jul. 2015.
- [45] D. M. Winker *et al.*, "The CALIPSO mission: A global 3D view of aerosols and clouds," *Bull. Amer. Meteorol. Soc.*, vol. 91, no. 9, pp. 1211–1229, Sep. 2010.
- [46] A. H. Omar *et al.*, "The CALIPSO automated aerosol classification and lidar ratio selection algorithm," *J. Atmos. Ocean. Technol.*, vol. 26, no. 10, pp. 1994–2014, Oct. 2009.
- [47] O. Torres, C. Ahn, and Z. Chen, "Improvements to the OMI near-UV aerosol algorithm using A-Train CALIOP and AIRS observations," *Atmos. Meas. Tech.*, vol. 6, no. 11, pp. 3257–3270, Nov. 2013.
- [48] S. Platnick *et al.*, "The MODIS cloud products: Algorithms and examples from Terra," *IEEE Trans. Geosci. Remote Sens.*, vol. 41, no. 2, pp. 459–473, Feb. 2003.
- [49] P. Ricchiazzi, S. Yang, C. Gautier, and D. Sowe, "SBDART: A research and teaching software tool for plane-parallel radiative transfer in the Earth's atmosphere," *Bull. Amer. Meteorol. Soc.*, vol. 79, no. 10, pp. 2101–2114, Oct. 1998.
- [50] "Remote Sensing Digital Image Analysis by John A Richards," NationalBookSeller.com, [Accessed: Oct. 30, 2014]. [Online]. Available: <http://www.nationalbookseller.com/510566/>
- [51] L. Liang, L. Di Girolamo, and S. Platnick, "View-angle consistency in reflectance, optical thickness and spherical albedo of marine water-clouds over the northeastern pacific through MISR-MODIS fusion," *Geophys. Res. Lett.*, vol. 36, no. 9, pp. 1–5, May 2009.
- [52] E. Kalnay *et al.*, "The NCEP/NCAR 40-Year Reanalysis Project," *Bull. Amer. Meteorol. Soc.*, vol. 77, no. 3, pp. 437–471, Mar. 1996.



**Ian Chang** received the B.S. degree in meteorology and the M.S. degree in geography (with an emphasis on satellite remote sensing and climatology) from Northern Illinois University, DeKalb, IL, USA, in 2010 and 2012, respectively. He is currently working toward the Ph.D. degree in the Department of Atmospheric Science, University of Alabama in Huntsville, Huntsville, AL, USA.

His Ph.D. research focuses on algorithm development, radiative forcing, diurnal cycle, and satellite validation of absorbing aerosols above clouds. He has taught undergraduate and graduate courses in satellite remote sensing, radiative transfer theory, atmospheric dynamics, and synoptic meteorology. He has published a manuscript entitled "A Global Climatology of Extreme Rainfall Rates in the Inner Core of Tropical Cyclones." His research areas encompass satellite remote sensing of aerosols and clouds, radiative transfer, tropical cyclone precipitation, and numerical modeling applications.

Mr. Chang is a member of the American Geophysical Union and the American Meteorological Society. He is a recipient of the 2015–2016 NASA Earth and Space Science Fellowship.



**Sundar A. Christopher** received the M.S. degree in meteorology from South Dakota School of Mines and Technology, Rapid, SD, USA, the M.S. degree in industrial/organizational psychology from the University of Alabama, Huntsville, AL, USA, and the Ph.D. degree in atmospheric sciences from Colorado State University, Fort Collins, CO, USA, in 1995.

He is a Professor of atmospheric science and the Dean of the College of Science, University of Alabama. His research interests include the role of aerosols and clouds on air pollution and climate. He enjoys teaching and has designed a professional development course for graduate students. His published book *Navigating Graduate School and Beyond: A Career Guide for Graduate Students* incorporates ideas from this course. He has published more than 100 papers in peer-reviewed journals and has presented his work at major scientific conferences, universities, and other organizations across the globe.